Supplemental Table and Figures

Table S1: Recording probes and locations per animal
Main dataset:

Animal	Types of probes implanted	Regions recorded
AB1	1 (256 sites, 8 shanks)[1]	CA1, CA3,DG
AB3	2 (256 sites, 8 shanks)	CA1,CA3,DG
AFR2	1 (256 sites, 8 shanks)	CA1,CA2,CA3,DG
AYA6	1 (256 sites, 8 shanks)	CA1,CA2,CA3,DG
AYA7	1 (256 sites, 8 shanks); 1 (256 sites, 4 shanks)[2]	CA1,CA2,CA3,DG,MEC
AYA9	1 (256 sites, 8 shanks); 1 (256 sites, 4 shanks)	CA1,CA2,CA3,DG,MEC
AYA10	1 (256 sites, 8 shanks); 1 (256 sites, 4 shanks)	CA1,CA2,CA3,DG,LEC
AYA2	1 (256 sites, 8 shanks); 2 (32 sites, 1 shank)	CA1,DG,MEC,LEC
AYA5	3 (32 sites, 1 shank)[3]	CA1,CA3,DG,MEC,LEC
AYA4	3 (32 sites, 1 shank)	CA1,CA3,DG,MEC,LEC
AFR1	3 (32 sites, 1 shank)	CA1,MEC,LEC

Data from AB1 and AB3 was used in previous works (Schomburg et al., 2014; Berényi et al., 2014; Oliva et al., 2016a/b) and data from AFR2, AYA2 and AYA6 in (Oliva et al., 2016a/b).
CNCRS.org hc3 dataset:
This dataset was only used for assessing phase-precession characteristics in the T-maze (Figure 6) and the
analysis of monosynaptically connected CA1 cell pairs (Figure 7)

Animal	Probes implanted	Regions recorded
ec012	1 (32 sites, 4 shanks)[4]	MEC
ec013	2 (32 sites, 4 shanks)	CA1,CA3,DG,MEC
ec014	1 (32 sites, 4 shanks); 1 (64 sites, 8 shanks) [4]	CA1,MEC
ec016	1 (32 sites, 4 shanks); 1 (64 sites, 8 shanks)	CA1,CA3,DG,MEC

1: Each shank of this probe has 32 electrode sites spaced 50 µm. Shanks are 300 µm spaced.
2: Each shank of this probe has 64 electrode sites spaced 25 µm in two rows ('staggered' configuration). Shanks are 200 µm spaced.
3: This probe has only one shank with 32 electrodes spaced 50 µm.
4: Each shank of this probe has 8 electrode sites spaced 15 µm in two rows ('stagger' configuration). Shanks are 200 µm spaced.

Table 1: Recording probes and their locations in each brain (Related to Figures 2 and 3)
Characteristics of silicon probes implanted in all animals and the anatomical regions recorded.

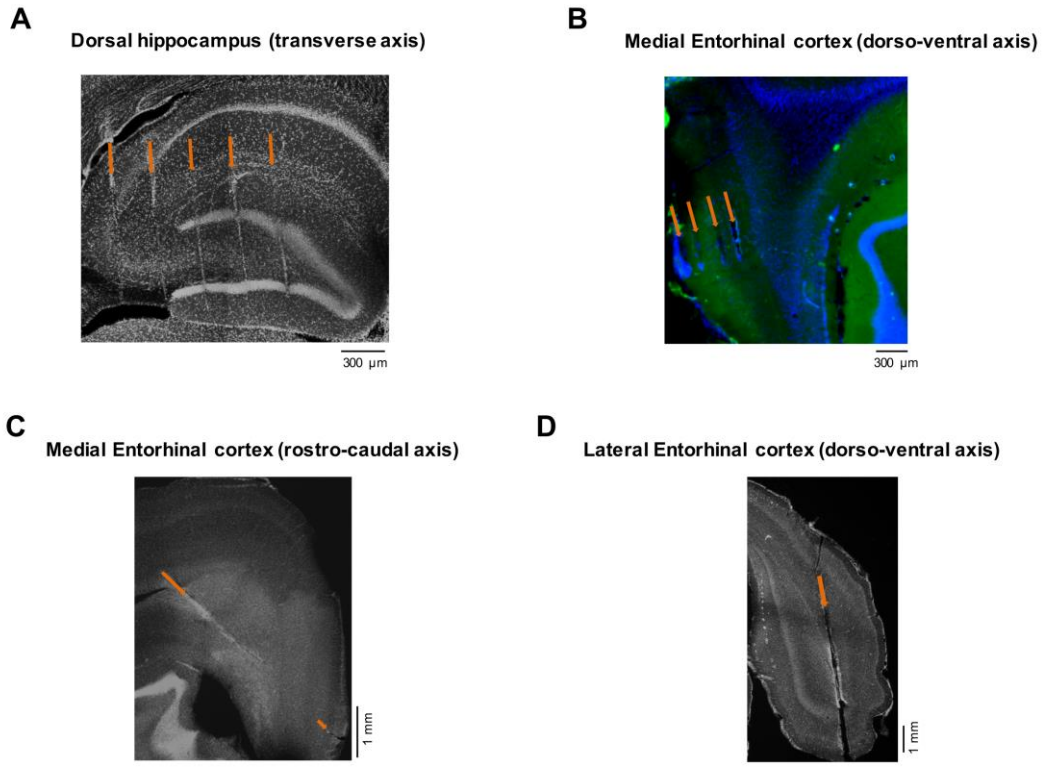

Figure S1: Histological verification of recording probe locations (Related to Figure 2)

(A) Eight-shank silicon probes (300 µm separation; 32 electrodes per shank with 50-µm spacing) were implanted parallel to the transverse axis of the dorsal hippocampus. The coordinates of the craniotomy (45° respect to the midline) were the following: -2.5 mm antero-posterior and 2.6 mm lateral from Bregma for the outer side and -4 mm antero-posterior and 0.8 mm lateral for the inner side. (**B**) Four-shank probes (200 µm separation; 64 electrodes in two rows per shank with 25-µm spacing) were implanted along the dorso-ventral axis of the medial entorhinal cortex. The probe was inserted 4.5 mm lateral, parallel to the midline with 25° degrees pointing anterior and the most caudal shank was inserted just rostral to the transverse sinus. In this configuration, each shank records activity from a different entorhinal layer. Calbindin inmuno-staining was used to identify layer II. (**C**) Single-shank probes (32 electrodes per shank with 50 µm spacing) were implanted along the rostro-caudal axis of the medial entorhinal cortex, approximately perpendicular to the cellular layers (-6.0 mm antero-posterior, 4.5 mm lateral, with a 25° angle in the sagittal plane pointing caudally). (**D**) Both types of probes (single-shank and four-shank) were also implanted along the dorso-ventral axis of the lateral-entorhinal cortex (8 mm antero-posterior, 5 mm lateral, 15° angle in the coronal plane pointing laterally). A track of a single-shank probe is shown here.

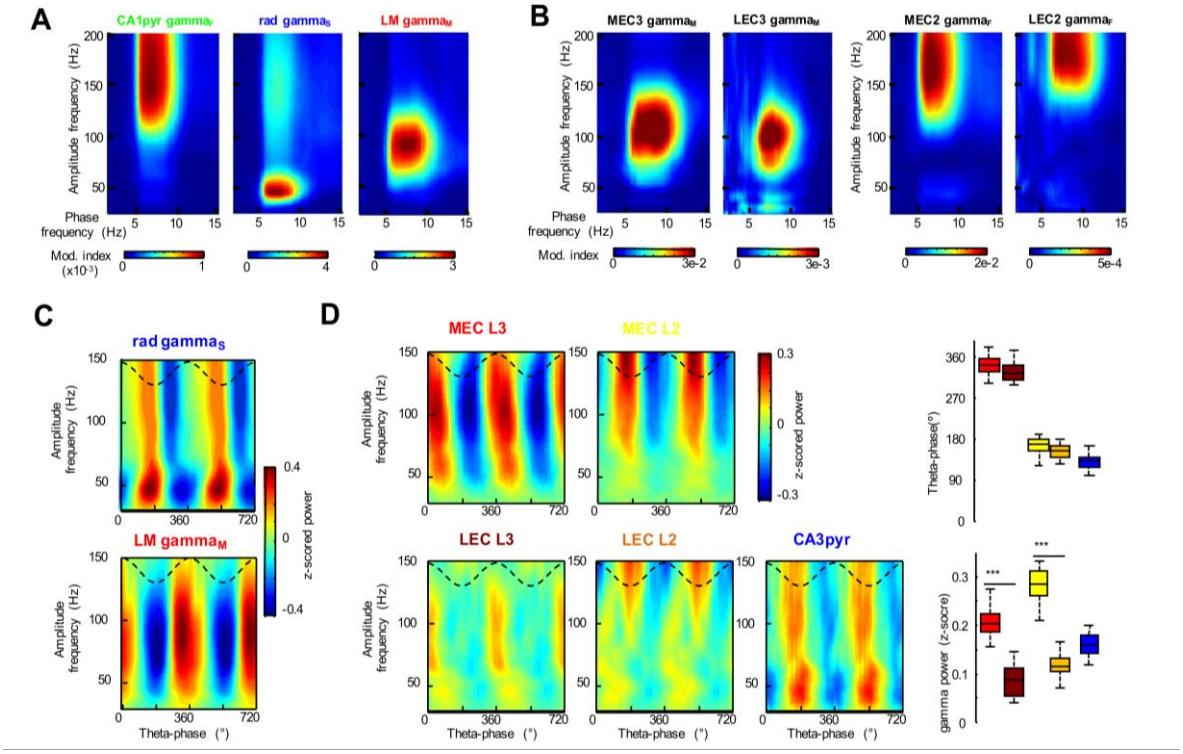

Figure S2: Theta-gamma dynamics in hippocampus and entorhinal cortices (Related to Figure 2 and 3)

(A) Gamma amplitude-theta frequency co-modulograms of the three main independent gamma components in CA1 LFP. Note that the three components display cross-frequency coupling in different gamma sub-bands (Schomburg et al., 2014). **(B)** Similar co-modulograms for LFP in layers II and III in the medial EC (MEC2, MEC3) and lateral EC (LEC2 and LEC3). Note the similar frequency of maximal theta-gamma coupling in the corresponding EC layers. Note also the considerable lower magnitude of gamma components in LEC (not different color scale, Modulation Index). (**C**) Average gamma amplitude – theta phase modulation plots for radiatum and LM components from he same session as the example in Figure 2A. (D) Average gamma amplitude – theta phase modulation plots for MEC2, 3 and LEC2, 3 layers and CA3 for one session. Right plots: Population theta phase preference and wavelet power of gamma oscillations in each region (mean ± SEM; *** $p < 0.001$, t-test).

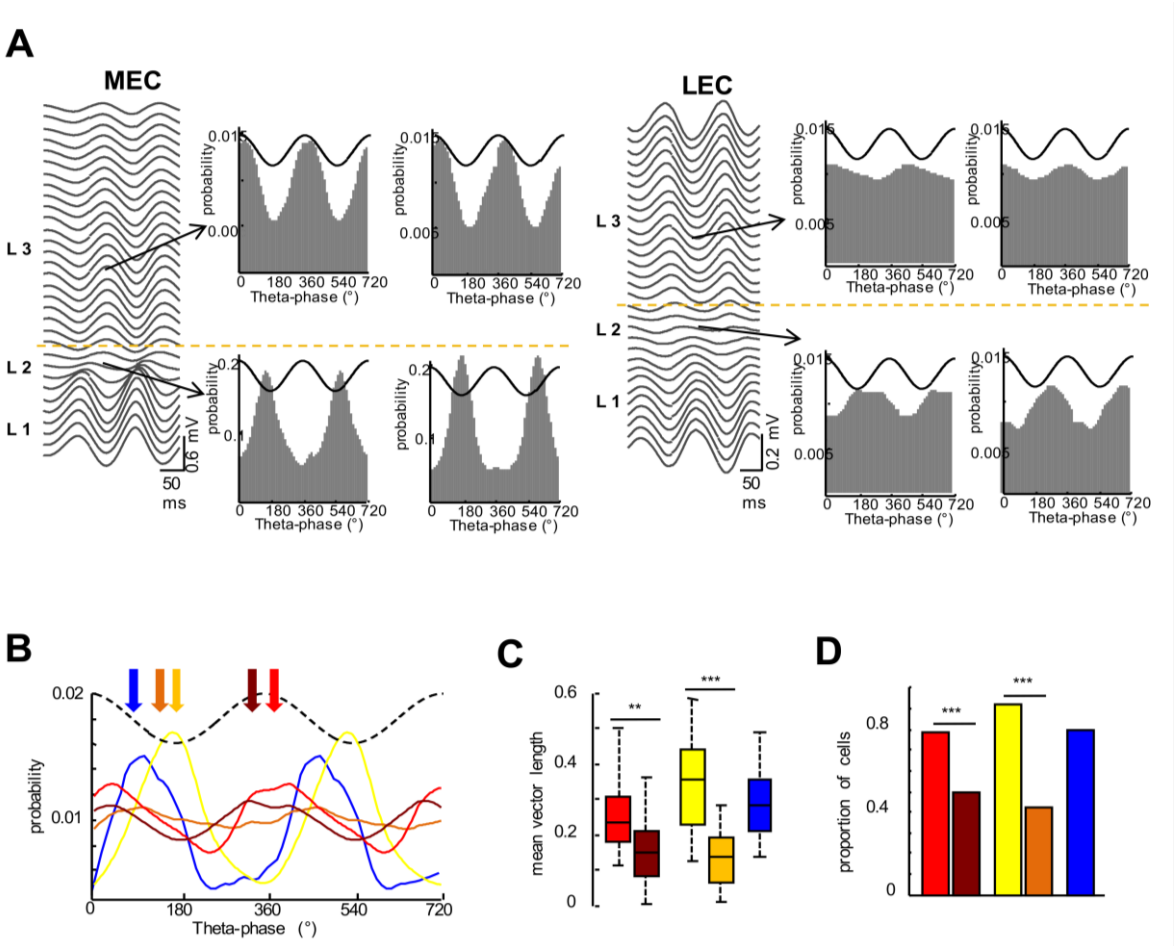

Figure S3: Theta-phase modulation of unit firing in MEC and LEC (related to Figures 2 and 3)

(A) Example LFP profiles of averaged theta waves in MEC and LEC. The reversal of theta waves indicates the boundary between entorhinal layers I and II (Mitchell and Ranck, 1980; Quilichini et al., 2010). Histograms of theta-phase spike probability distributions of representative units in MEC and LEC. Note the opposite theta phase preference of EC2 and EC3 units (Mizuseki et al., 2009) and the lower theta modulation of LEC units. (**B**) Distribution of preferred theta phases for all excitatory units in different entorhinal layers and CA3 during maze running (RUN). Note the opposite phase preference of layer 2 (EC2) and 3 (EC3) entorhinal excitatory cells. Color arrows indicate peaks in discharge probability distributions for each group. (**C**) Strength of theta modulation (mean vector length) for the different populations of cells. (**D**) Total percentage of theta modulated cells ($p < 0.05$ Rayleigh test).

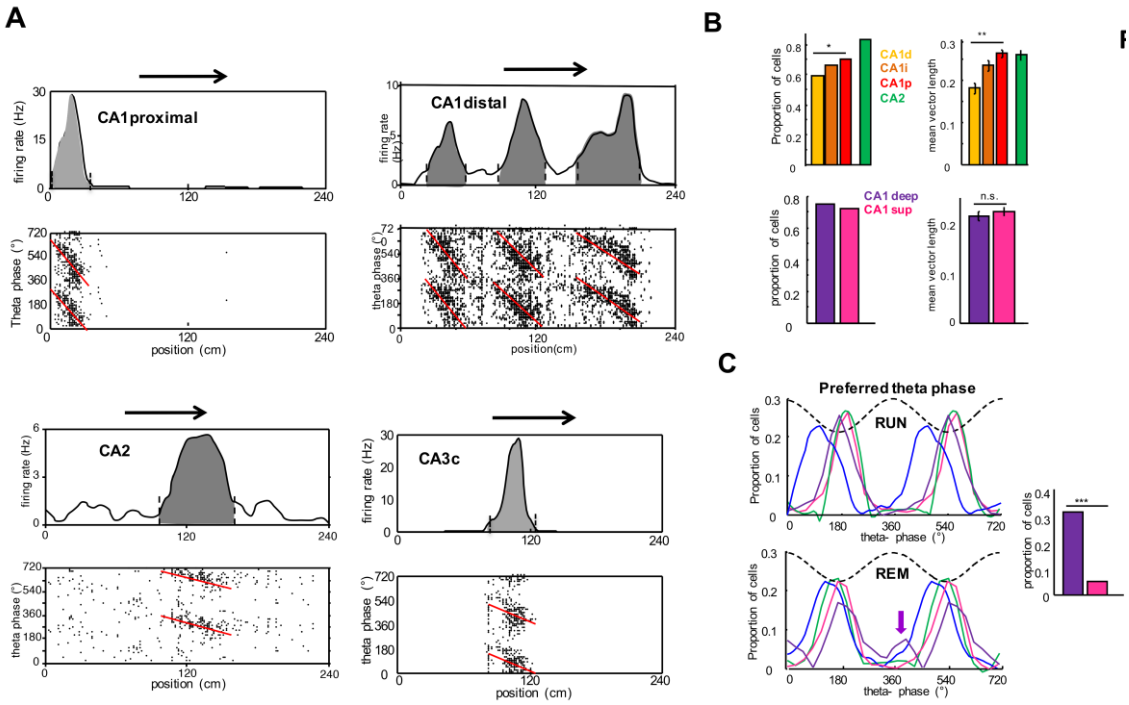

Figure S4: Characteristics of phase-precession and spike theta-phase modulation across hippocampal regions (Related to Figures 2 and 3)

(A) Examples of phase-precessing place cells from different regions. Note the wider phase range of CA1 place cells compared to CA2 and CA3 neurons. **(B)** Proportion of significantly theta-modulated pyramidal cells ($p < 0.01$ Rayleigh test) and strength of theta modulation (mean vector length), shown separately for the three different subregions of CA1, CA2 (upper plot) and deep and superficial CA1 sublayers (bottom). **(C)** Distribution of preferred theta phases in pyramidal cells in different regions, subregions and sublayers. Note that a fraction of CA1 deep layer cells shifted their preferred phase towards the theta peak during REM compared to RUN (purple arrow) (Mizuseki et al., 2011). Color-coding as in B.

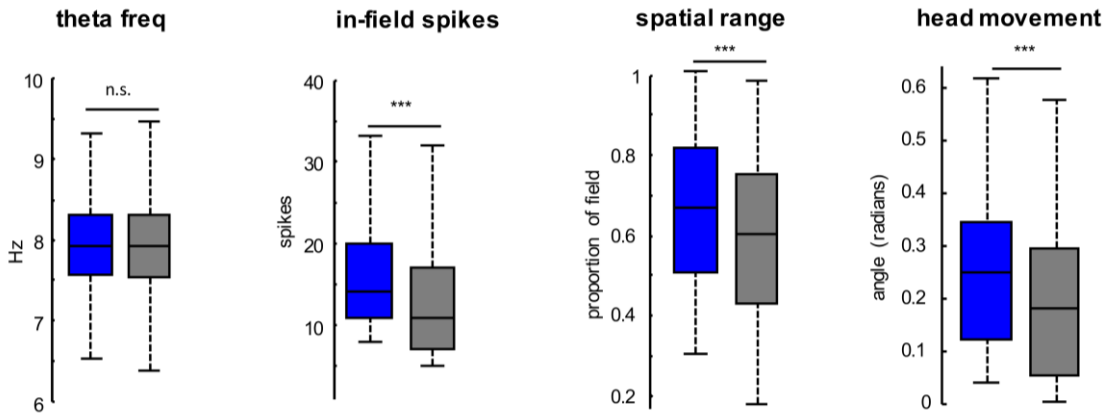

Figure S5: Comparison of behavioral and physiological parameters during strongly versus weakly precessing trials (Related to Figure 4)

Theta frequency was similar in both types of trials. In-field number of spikes, spatial range (single trial place field size compared to pooled trials field size) and lateral head movements were significantly larger in strongly compared to weakly precessing trials. *** $p < 0.05/0.01/0.001$ rank-sum test.

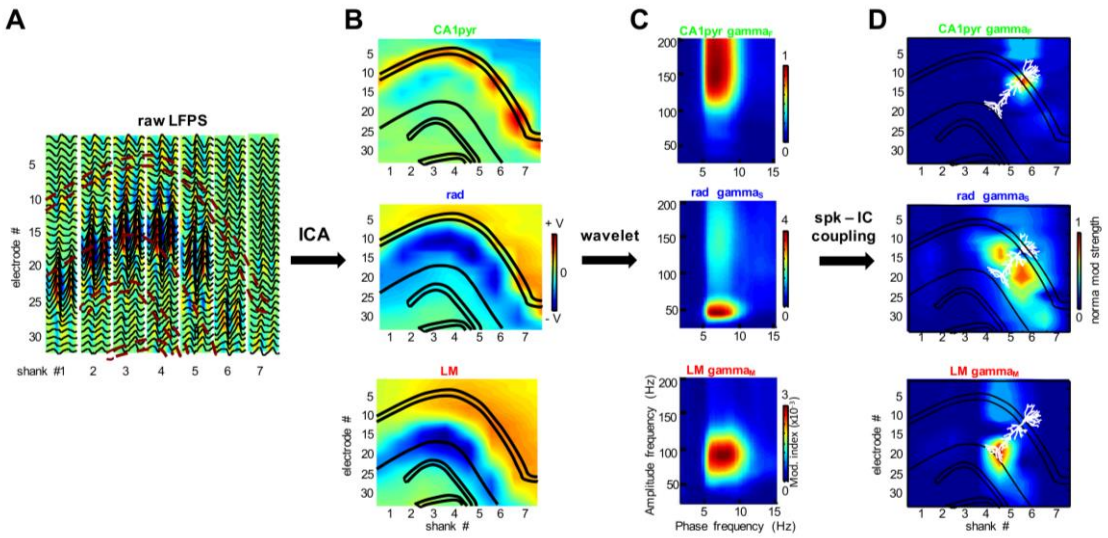

Figure S6: Isolation of layer-specific synaptic inputs to individual cells (Related to Figure 5)

(A) Procedure followed for the analysis of gamma inputs to individual cells. Averaged LFP theta and CSD profiles recorded during running in the linear track with a 256-site electrode placed parallel to the transversal axis of the hippocampus. **(B)** LFP was filtered (30 - 200 Hz) and Independent Component Analysis (ICA; Fernandez-Ruiz et al., 2012a) was applied to LFP recorded from each site to identify three main local sources of gamma oscillations (Fernandez-Ruiz et al., 2012a; Mizuseki et al., 2012; Quilichini et al., 2010). Backprojecting ICs voltage loadings to the electrode anatomical space results in 2D maps revealing the layer specificity of each IC. (This figure is reproduced from Figure 1 D of (Schomburg et al., 2014)). CA1 pyramidal layer (CA1pyr), stratum radiatum (rad) and stratum lacunosum – moleculare (LM). (**C**) High frequency activity of each IC was decomposed by means of complex wavelet transform (from 25 to 200 Hz). Gamma amplitude-theta frequency analysis revealed coupling of each IC in a specific gamma sub-band: $gamma_F$ (100- 200 Hz), $gamma_S$ (30 - 60 Hz) and $gamma_M$ (60 -110 Hz) (Schomburg et al., 2014). (**D**) For each neuron, spike - LFP phase-coupling at every wavelet step was calculated for each IC at all 256 recording sites. The maximal spike-LFP coupling in each of the three gamma sub-bands reliably aligned with the anatomical position of cell soma and the dendritic strata of the putative apical dendrites with respect to the recording electrode. Note that, due to the curvature of the hippocampal layers, different dendritic layers of the same projected cell were recorded from different shanks. Projected pyramidal cells dendrites are shown here for illustration only. Verification of the validity of the single cell projection method will require future experiments with combined spike-LFP coupling and intracellular recording/labeling of neuronal morphology.

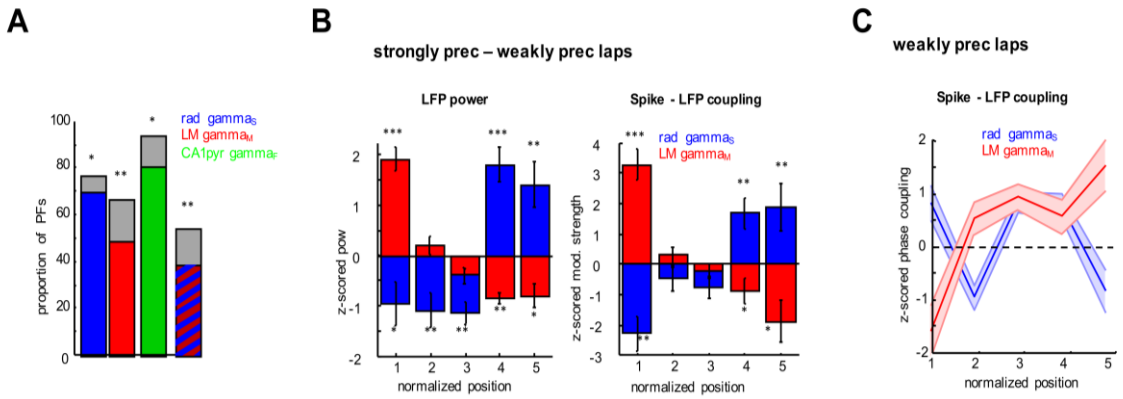

Figure S7: Within-place field dynamics during strongly versus weakly precessing trials (Related to Figure 5)

(A) Proportion of all place fields with significant ($p < 0.01$, Rayleigh test) spike-gamma oscillatory phase-coupling, shown separately for the three gamma sub-bands (color bars). Striped bar: place fields with significant phase modulation by both $gamma_S$ and $gamma_M$. Only place fields with non-significant phase-precession ($n = 219$; $p > 0.05$, circular-linear correlation) were included. Compare to place fields with significant phase precession (grey bars and Figure 5B; $n = 309$; $r^2 > 0.1$, $p > 0.05$, circular-linear correlation). A smaller proportion of weakly precessing place fields had phase-coupling to each gamma oscillation band, but specially with LM $gamma_M$ compared to phase precessing place fields */** $p < 0.05/0.01$ χ -square test. **(B)** To compare within-place field gamma inputs to the place cell firing during strongly versus weakly precessing trials, we calculated, for each place cell, the difference of spike-sampled gamma power (left plot) and spike phase-coupling (right) for both types of trials in each bin of the place field. Str. radiatum (rad) $gamma_S$ (blue) power and spike phase-coupling were lower at the entrance of the field and higher at the exit for strongly precessing trials compared with weakly precessing ones. LM $gamma_M$ (red) power and phase-coupling were higher at the entrance of the field and lower at the exit for strongly precessing trials compared with weakly precessing ones. */**/*** $p < 0.05/0.01/0.001$ rank-sum test.

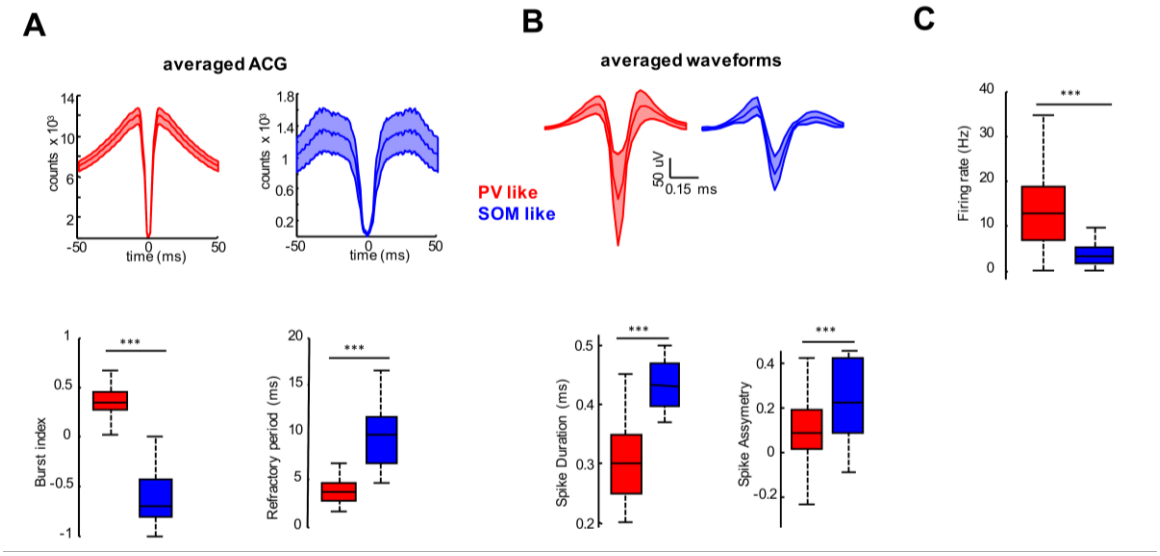

Figure S8: Physiological classification of interneuron subtypes (Related to Figure 6)

(A) Top: Averaged autocorrelograms for all PV-like (red; n = 618) and SOM-like (blue; n = 141) interneurons. Autocorrelogam (ACG) characteristics were quantified by calculating a burst index and refractory period (see Methods). Bottom: PV-like cells were more bursty and had shorter refractory periods compared to SOM-like cells. **(B)** Top: averaged waveforms for both types of interneurons. Waveform characteristics were characterized by calculating spike duration and asymmetry. PV-like cells had shorter and less asymmetric waveforms compared to SOM-like cells. **(C)** PV-like interneurons had higher global firing rates than SOM-like interneurons. Interneurons that could not be classified as belonging to one of these two groups were excluded from all analysis (n = 56). *** p < 0,001, rank-sum test.